Magnetic anisotropy in ferromagnetic CrI_3

Lebing Chen,[1] Jae-Ho Chung,[2,*] Tong Chen,[1] Chunruo Duan,[1] Astrid Schneidewind,[3] Igor Radelytskyi,[3] David J. Voneshen,[4] Russell A. Ewings,[4] Matthew B. Stone,[5] Alexander I. Kolesnikov,[5] Barry Winn,[5] Songxue Chi,[5] R. A. Mole,[6] D. H. Yu,[6] Bin Gao,[1] and Pengcheng Dai[1,†]

[1]*Department of Physics and Astronomy, Rice University, Houston, Texas 77005, USA*
[2]*Department of Physics, Korea University, Seoul 02841, Korea*
[3]*Forschungszentrum Jülich GmbH, Jülich Centre for Neutron Science (JCNS) at Heinz Maier-Leibnitz Zentrum (MLZ), Lichtenbergstrasse 1, 85748 Garching, Germany*
[4]*ISIS Pulsed Neutron and Muon Source, STFC Rutherford Appleton Laboratory, Harwell Campus, Didcot, Oxon, OX11 0QX, United Kingdom*
[5]*Neutron Scattering Division, Oak Ridge National Laboratory, Oak Ridge, Tennessee 37831, USA*
[6]*Australian Nuclear Science and Technology Organisation, Locked bag 2001, Kirrawee DC, NSW 2232, Australia*

(Dated: March 14, 2020)

We use neutron scattering to show that ferromagnetic (FM) phase transition in the two-dimensional (2D) honeycomb lattice CrI_3 is a weakly first order transition and controlled by spin-orbit coupling (SOC) induced magnetic anisotropy, instead of magnetic exchange coupling as in a conventional ferromagnet. With increasing temperature, the magnitude of magnetic anisotropy, seen as a spin gap at the Brillouin zone center, decreases in a power law fashion and vanishes at T_C, while the in-plane and c-axis spin-wave stiffnesses associated with magnetic exchange couplings remain robust at T_C. These results suggest that the SOC induced magnetic anisotropy plays a dominant role in stabilizing the long range FM order in single layer 2D van der Waals ferromagnets.

INTRODUCTION

Understanding the microscopic origin of two-dimensional (2D) ferromagnetic (FM) order and spin dynamics in van der Waals materials is important for their potential magnet-based applications [1]. In a conventional three-dimensional (3D) cubic spin-rotation invariant (spin isotropic) ferromagnet, the Curie temperature T_C associated with the second order FM phase transition is determined by the short range magnetic exchange coupling J [2]. In the low wave-vector ($q \to 0$) limit, spin-wave energies E follow the well-known quadratic dispersion relation $E = \Delta(T) + D(T)q^2$, where $D(T)$ [$D(T \to 0) \propto J$] is the spin-wave stiffness and $\Delta(T)$ is a vanishingly small dipolar gap [2]. The quadratic dispersion form, however, is general for any ferromagnet and not limited to the Heisenberg model [2]. According to the hydrodynamic and mode-mode coupling theories, temperature dependence of the spin-wave stiffness in a second order FM phase transition must vanish at T_C via $D(T) \propto (1 - T/T_C)^{\nu-\beta}$, where ν and β are critical exponents of the magnetic phase transition [3, 4]. For a typical 3D Heisenberg ferromagnet, we expect $(\nu - \beta) = 0.34$ comparing with the measured values for iron (0.36 ± 0.03), cobalt (0.39 ± 0.05), and nickel (0.39 ± 0.04) [4]. When the dimensionality of the magnetic system is reduced from 3D to 2D, Mermin and Wagner showed the absence of long-range FM or antiferromagnetic (AF) order at finite temperature in spin-rotational invariant systems with short-range magnetic interactions [5]. Although the long-range FM order in 2D systems at finite temperature can be brought about by breaking the spin-rotational invariance [6], the ordering temperature is again expected to be determined by J, resulting $D(T) \to 0$ at T_C [1, 4, 6, 7]. Therefore, the discovery of robust FM order in van der Waals monolayers of CrI_3 [8] and $Cr_2Ge_2Te_6$ [9] raised an important question concerning the magnetic interactions that break the spin-rotational invariance and stabilize the finite temperature 2D FM order.

In principle, spin rotational invariance of a 3D magnetic system can be broken via dipolar interactions [10], single-ion (magnetocrystalline) anisotropy [11], and/or anisotropic magnetic exchange interactions [12, 13]. For layered honeycomb lattice ferromagnet such as CrI_3 [Figs. 1(a,b)] [14], another possible mechanism that can break spin rotational invariance is the off-diagonal term Γ in the Heisenberg-Kitaev (J-K-Γ) Hamiltonian [Fig. 1(c)] [15–23]. For bulk CrI_3, which orders ferromagnetically below $T_C = 61$ K, the FM order is believed to be a second order phase transition [14]. In addition, there is a strong magnetic anisotropy revealed as a large difference in the saturation magnetic field for field parallel to the c-axis direction (H_c^S) and in the ab plane (H_{ab}^S and $H_{ab}^S - H_c^S \approx 3$ T) [14, 24]. By comparing the temperature dependence of the magnetic anisotropy of CrI_3 with those of $CrBr_3$, it was concluded that the magnetic anisotropy in CrI_3 arises from a dominant uniaxial or single-ion anisotropy [24], which comes mostly from the interplay between spin-orbit coupling (SOC) of the Cr magnetic ion with the crystal electric field (CEF) levels induced by its surrounding I atoms arranged in an edge sharing octahedra [Figs. 1(c,d)]. Since dipolar interactions typically are very small and favor in-plane anisotropy [10], its effects on spin rotation anisotropy is negligible and can be safely ignored [12, 13]. On the other hand, single-ion anisotropy in CrI_3 has been estimated to be way below 1 meV because of the quenched orbital moment of Cr^{3+} and the large energy separation ($\approx$500 meV) of the CEF excited states of the Cr^{3+} ion [Figs. 1(c,d)] [12, 13]. Finally, spin rotational invariance of a magnetic system such as CrI_3 can be broken because of the magnetic anisotropy arising from the Cr 3d-I p-Cr 3d superexchange hopping in the near 90° bonding angle networks [Fig. 1(c)] [12, 13].

If magnetism in 3D CrI_3 also breaks the spin rotational invariance and becomes anisotropic in real space, it should reveal itself as a gap in spin-wave dispersion at the Γ point in Fig. 1(b) with $\Delta > 0$, in contrast to the $\Delta \approx 0$ seen in typical isotropic ferromagnets [25, 26]. In principle, one can detect such a gap by FM resonance [27], Raman scattering [28], or inelastic neutron scattering (INS) [25, 26]. Using FM resonance [29], a spin gap of $\sim$0.3 meV was estimated at the Γ point below T_C [18]. On the other hand, polarized micro-Raman spectroscopy experiments on CrI_3 found evidence for two sets of zero wave-vector spin waves at 9.4 meV and 15.5 meV [30]. Since CrI_3 has two magnetic ions per unit cell, giving rise to only one acoustic and one optical spin-wave branches [18, 30, 31], the Raman spectroscopy results suggest a spin gap of 9.4 meV at the Γ point [30]. Finally, INS experiments on single crystals of CrI_3 revealed a $\sim$4 meV spin gap at the Dirac (K) points but found no evidence of a spin gap above $\sim$1 meV at the Γ point [31]. While FM resonance [18] and INS [31] results are clearly in contrast to those of Raman spectroscopy [30], the actual value of the anisotropy gap is still undetermined. To conclusively determine the size of the spin gap and its temperature dependence, and test if spin dynamics in CrI_3 are consistent with a Heisenberg ferromagnet [4], INS experiments are necessary.

RESULTS

In this paper, we report INS studies of spin waves in CrI_3. In addition to confirming a spin gap of $\Delta = 0.37 \pm 0.02$ meV at $T = 3$ K and the Γ point, we trace the temperature dependence of $\Delta(T)$ and $D(T)$ across T_C. While spin-wave

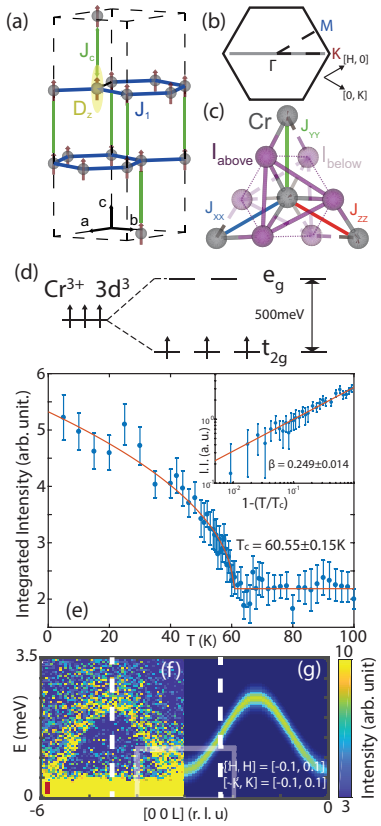

FIG. 1. (a) Crystal structure of CrI_3, where the nearest neighbor magnetic exchange couplings within the Cr-plane and along the c-axis are J_1 and J_c, respectively. The D_z is the single-ion anisotropy. (b) Reciprocal space within the $[H, K]$ plane, where Γ, K, M points are specified. The gray line indicates the $\mathbf{Q}$-direction for constant-energy scans. (c) Real space picture of CrI_3, where the nearest-neighbor I atoms form an octahedral environment with 3 I above (dark purple) and 3 I below (light purple) the Cr layer. The Cr-I-Cr path forms an angle close to 90 degrees [12, 13]. The Kitaev interactions between Cr^{3+} atoms are marked as J_{xx}, J_{yy}, and J_{zz} [18]. (d) The CEF level of the I octahedra splits the d levels in the e_g and t_{2g} manifolds. (e) Magnetic order parameter at the $(1, 1, 0)$ position. The inset is a log-log plot of the integrated magnetic peak intensity. Both red lines are power law fits with the same critical exponent $\beta = 0.249 \pm 0.014$. (f) Spin-wave dispersion along the $[0, 0, L]$ direction at $T = 3$ K obtained with $E_i = 5.2$ meV. (g) The Heisenberg model fit of the c-axis dispersion. The dashed lines in (f,g) indicate const-$\mathbf{Q}$ scans in Figs. 2(c,d). Red bars in (f), Figs. 2(a,c,d,e), 3(e), and 4(a) are instrumental energy resolution [23].

stiffness within the CrI_3 plane $D_{HH}(T)$ is considerably larger than that of the stiffness along the c-axis $D_L(T)$, they both do not vanish at T_C, contrary to the expectation of a 3D [3, 4] or 2D [1, 6, 7] Heisenberg ferromagnet with a second order FM phase transition. On the other hand, the anisotropy gap $\Delta(T)$ has an order-parameter-like temperature dependence and vanishes at T_C. These results, together with the lack of magnetic critical scattering around T_C, suggest that the FM phase transition in CrI_3 is weakly first order instead of a second order phase transition. We thus conclude that the breaking of the spin-rotation invariance via large SOC is ultimately responsible for stabilizing the FM order in 3D and monolayer CrI_3, and other monolayer materials [32–36].

Our INS measurements were performed on single crystals and powders of CrI_3 using spectrometers at ISIS [Figs. 1(f), 2(a,b)] [37, 38], Heinz Maier-Leibnitz Zentrum [Figs. 2(c,d)] [39], ANSTO [Figs. 2(e,f)] [40], and ORNL [Figs. 1(e), 3, 4] [41, 42]. Using a honeycomb structure with in-plane Cr-Cr distance of $a = b \approx 3.96$ Å and c-axis layer spacing of $c = 6.62$ Å in the low temperature rhombohedral structure [Fig. 1(a)] [43], the momentum transfer $\mathbf{Q} = H\mathbf{a}^* + K\mathbf{b}^* + L\mathbf{c}^*$ is denoted as $\mathbf{Q} = (H, K, L)$ in reciprocal lattice units (r.l.u.) [Fig. 1(b)] [31].

In an ionic picture, Cr^{3+} in CrI_3 has an electronic configuration $3s^0 3d^3$ and is surrounded by 6 I atoms in an octahedral environment [Fig. 1(c)]. The d levels of Cr^{3+} split into a higher energy e_g doublet and a lower energy t_{2g} triplet separated by ∼500 meV [Fig. 1(d)] [12]. With the first Hund rule, 3 electrons in Cr^{3+} occupy the t_{2g} manifold in the $S = 3/2$ state with quenched orbital moment $\langle \vec{L} \rangle \simeq 0$ [Fig. 1(d)] [12, 13]. Figure 1(e) shows temperature dependence of the $(1, 1, 0)$ Bragg peak intensity, confirming the FM transition at $T_C = 60.5 \pm 0.2$ K. The solid line

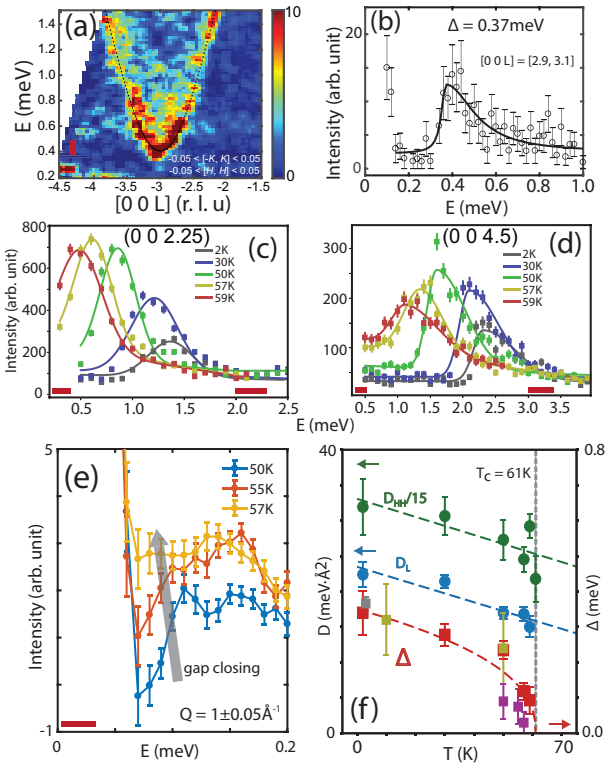

FIG. 2. (a) Images of spin waves near the Γ point. The red box shows the integration range in (b). (b) An energy cut of the data at $\mathbf{Q} = (0, 0, -3)$. (c) Constant-$\mathbf{Q}$ scans for $\mathbf{Q} = (0, 0, 2.25)$. (d) Similar scans at $\mathbf{Q} = (0, 0, 4.5)$. (e) Temperature dependence of the spin gap around the Γ point [23]. (f) Temperature dependence of the $D_{HH}(T)$ (green dots), $D_L(T)$ (blue squares), and $\Delta(T)$ (different colored squares), where the dashed line is a fit to the power law equation. The green and blue dashed lines are guides to the eye.

in the figure is a fit to the magnetic order parameter by $I = I_0(1 - T/T_C)^{2\beta}$ [4]. Within the temperature range probed, we find $\beta = 0.25 \pm 0.01$ [Inset in Fig. 1(e)]. This value is in-between the critical exponents of 2D and 3D Ising ferromagnets [4, 44], thus suggesting finite interplanar (c-axis) magnetic exchange coupling J_c in CrI_3. This is consistent with the spin-wave dispersion along the c-axis at $T \approx 3$ K [Fig. 1(f)]. Figure 1(g) shows a fit to the spin-wave dispersion using a Heisenberg Hamiltonian [31].

Figure 2(a) shows spin waves near the Γ point, revealing an anisotropy gap of $\Delta = 0.37 \pm 0.02$ meV at $T = 3$ K. An energy cut at the spin-wave minimum indicates step-like intensity gain around 0.37 meV [Fig. 2(b)]. While the magnitude of Δ is smaller by a factor of two compared with estimation from previous measurements [31], it is consistent with estimation from the FM resonance [18, 29] and larger than in its isostructual compound $CrBr_3$ ($\Delta < 0.1$ meV) [45] and $CrSiTe_3$ ($\Delta \approx 0.075$ meV) [46], suggesting considerably stronger SOC in CrI_3.

To determine the temperature dependence of the magnetic exchange couplings within the CrI_3 plane and along the c-axis, we measured spin-wave dispersions around the Γ point along the intraplanar $[H, H, 3]$ [23] and interplanar $[0, 0, L]$ directions. Figures 2(c,d) are the constant-$\mathbf{Q}$ scans to probe the temperature dependence of interplanar modes for temperatures up to $T = 59$ K ($= 0.97T_C$). Since the full interplanar spin-wave bandwidth could be observed [Fig. 1(f)], we performed variable-energy scans at $\mathbf{Q} = (0, 0, 2.25)$ [Fig. 2(c)] and $(0, 0, 4.5)$ [Fig. 2(d)]. The zone boundary spin-wave energy at $T = 0.97T_C$ is reduced by ∼50% [Fig. 2(d)], suggesting significant interplanar exchanges approaching the FM transition. Assuming that the interplanar dispersion follows the simple sinusoidal dependence on L [Fig. 1(f)], we can estimate the spin wave stiffness along the c-axis $D_L(T) \equiv a_L(T)(c/6)^2$ in units of meVÅ^2 by fitting the data with $E = a_L(T)\left[\sin\left(\frac{\pi}{3}L\right)\right]^2 + \Delta(T)$. Figure 2(e) shows temperature dependence of spin gap around the Γ point ($|\mathbf{Q}| = 1 \pm 0.05$ Å^{-1}) approaching T_C [23]. Figure 2(f) summarizes temperature dependence of the in-plane $[D_{HH}(T)]$ [23] and c-axis $[D_L(T)]$ spin wave stiffnesses, revealing that the intraplanar and interplaner exchange couplings almost fully active up to T_C in spite of the vanishing magnetization at T_C in Fig. 1(e). In contrast, $\Delta(T)$ obtained from the c-axis dispersion and direct measurements vanishes at T_C [see right axis in Fig. 2(f)] [23]. The dashed line shows a fit to the data using $\Delta(T) \propto (1 - T/T_C)^{\nu-\beta}$, giving $\nu - \beta = 0.35 \pm 0.14$.

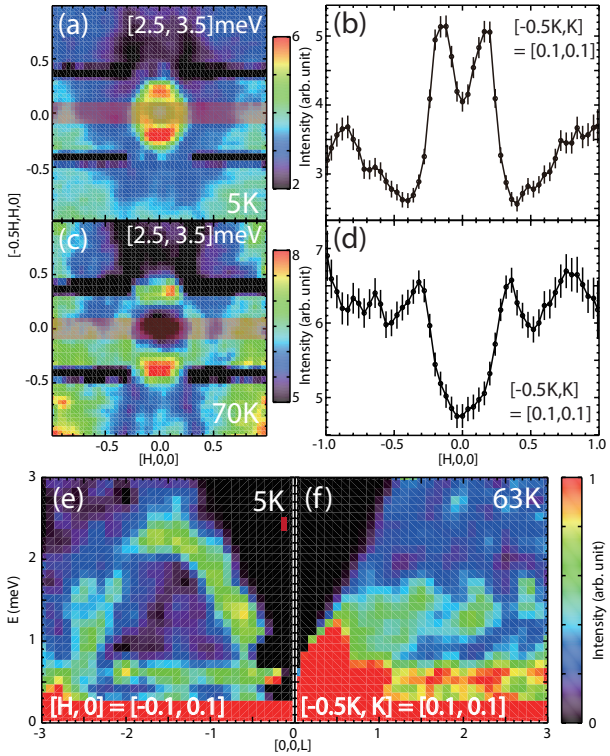

FIG. 3. (a) Low energy ($E = 3 \pm 0.5$ meV) spin waves of CrI_3 in the $[H, K]$ plane at $T = 5$ K. (b) A cut along the $[H, 0]$ direction. (c) The same scan as (a) but at $T = 1.14T_C$. (d) The same cut as (b) at $T = 1.14T_C$. The red boxes in (a,c) show the integration range in (b,d), respectively, with L integrated from $[-5, 5]$. (e) Spin wave dispersion along the c-axis at $T = 5$ K. (f) Identical scan at $T = 1.03T_C$. The data was collected using $E_i = 8$ meV [23].

At temperatures above T_C, spin excitations of CrI_3 become diffuse but still have signatures of the intraplanar modes. Figures 3(a) and 3(c) are images of the constant-energy slices ($E = 3.0 \pm 0.5$ meV) at $T = 5$ K and 70 K, respectively [23]. We see clear spin-wave-like rings in the $[H, K]$ plane at both temperatures although the excitations are noticeably diffusive at $T = 70$ K ($= 1.14T_C$). **Q**-dependent cuts through data in Figs. 3(b) and 3(d) bear this out, showing some softening of the in-plane spin-wave energy on warming but is non-vanishing at T_C. Figures 3(e) and 3(f) show similar data along the c-axis, where we see considerable yet incomplete (∼50 %) softening of the mode above T_C. Therefore, FM order in CrI_3 is not determined by the in-plane or c-axis magnetic exchange interactions as in a conventional 3D Heisenberg ferromagnet [4]. It is also different from the expectation of an ideal 2D Heisenberg ferromagnet [1, 6, 7].

To understand why $D(T)$ does not vanish at T_C in CrI_3 as required by the mode-mode coupling theory in a Heisenberg ferromagnet with second order phase transition [4], we consider the nature of the FM phase transition. In a second order FM phase transition, spin-spin correlation length and magnetic critical scattering should diverge at T_C [4]. Figure 4(a) compares the magnetic Bragg peak across the $(1, 1, 0)$ reflection at 10 K with the instrumental resolution obtained by measuring the same nuclear Bragg peak above T_C. The magnetic Bragg peak width is clearly broader than the nuclear Bragg peak width, indicating that the spin-spin correlation length is not resolution-limited. Temperature dependence of the magnetic scattering around the $(1, 1, 0)$ reflection in triple-axis mode reveals no peak above T_C [Fig. 4(b)], suggesting the lack of critical scattering around T_C. Figure 4(c) shows temperature dependence of the $(1, 1, 0)$ peak width. At temperatures above T_C, the $(1, 1, 0)$ peak width measures nuclear lattice correlation, which is the instrumental resolution-limited. On cooling below T_C, we see a clear broadening of the width that saturates below about 53 K, indicating that the in-plane spin-spin correlations in CrI_3 are short-ranged even at 10 K and never reached the instrumental resolution (nuclear Bragg peak width) [Fig. 4(c)]. Temperature dependence of the inelastic scattering at $E = 1.4$ meV shows no anomaly at T_C, again suggesting no critical magnetic scattering.

While these results suggest that the FM phase transition in CrI_3 may be weakly first order instead of second order [14], a more stringent test is to measure the instantaneous spin correlations in CrI_3 across T_C [47]. In these two-axis neutron scattering measurements, the final neutron wave vector is aligned along the c-axis direction throughout the scan and all final neutron energies are integrated [Fig. 4(e)]. For a classical second order phase transition, we expect

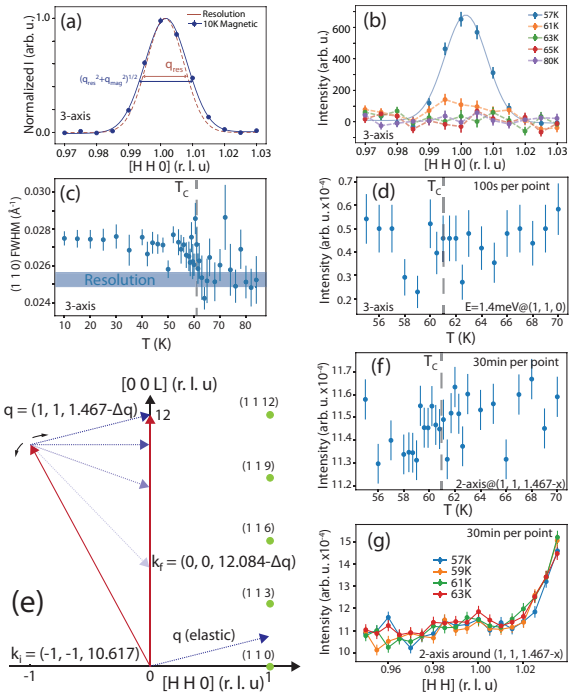

FIG. 4. (a) Wave vector dependence of the magnetic Bragg peak $(1,1,0)$ along the $[H,H,0]$ direction obtained by subtracting the nuclear Bragg peak above T_C from the same scan at 10 K. The dashed line is the instrument resolution limited nuclear Bragg peak above T_C (80 K to 84 K). The data was collected on HB-3 with collimation of 40′-40′-40′-120′ and final neutron energy of $E_f = 14.7$ meV. The blue line is a fit to Gaussian on a flat background, giving spin-spin correlation length of 220 ± 4 Å. (b) Temperature dependence of the magnetic scattering around the $(1,1,0)$ position across T_C, where high temperature nuclear Bragg peak is subtracted. (c) Temperature dependence of the full-width-half-maximum (FWHM) of the $(1,1,0)$ peak across T_C. Above T_C, the FWHM shows instrumental resolution limited nuclear Bragg peak width. (d) Temperature dependence of the inelastic scattering at $E = 1.4$ meV and $(1,1,0)$. (e) Schematics of the two-axis mode scan with neutron final wave vector $k_f||c$. The incident neutron energy E_i is fixed at 30.5 meV. The scattering intensity shown in (f) and (g) is integrated over all possible k_f. (f) Temperature dependence of the scattering at in-plane wave vector $(1,1,0)$. (g) $[H,H,0]$ scans across the in-plane wave vector $(1,1,0)$ around T_C using two-axis mode. The intensity obtained in (f) and (g) is an integration over all possible values of Δq.

to observe critical spin fluctuations as a peak in the instantaneous spin correlations at the $(1,1,0)$ position, and the peak intensity should diverge on approaching T_C from high temperature. However, the temperature dependence of the scattering at the $(1,1,0)$ position reveals no anomaly across T_C [Fig. 4(f)]. The wave vector dependence of the scattering at various temperature across T_C also shows no obvious peak at the $(1,1,0)$ position. If we assume that the FM phase transition in CrI_3 is indeed weakly first order instead of second order, we can understand the c-axis lattice distortion associated the FM phase transition [14] and the peak in FM transition induced heat capacity anomaly [48]. The first order nature of the FM transition in CrI_3 provides a natural understanding for nonvanishing values of $D(T)$ at T_C, suggesting that FM order is not controlled by the magnetic exchange interaction in contrast to a Heisenberg Hamiltonian [4].

DISCUSSION

The direct relation between the magnetic anisotropy and FM phase transition is revealed in the similar temperature dependence of the spin gap $\Delta(T)$ in Fig. 2(f) and magnetic order parameter in Fig. 1(e). The c-axis component of the ordered moment, S^z, is included in the anisotropic interaction term of the nearly-isotropic Heisenberg Hamiltonian $H = -\Sigma_{i>j} J_{ij}\mathbf{S}_i \cdot \mathbf{S}_j - \Sigma_{<ik>} A_{ik} S_i^z S_k^z$, where $\mathbf{S}_i$ is the spin on site i. The A_{ik} in the second term accounts for the single-ion anisotropy or anisotropic exchange constant, with c being the easy axis, when the summation is over $i = k$ or $i > k$, respectively. If the anisotropic exchanges are limited to the nearest-neighbor bonds, the linear spin-wave energies calculated using $A_{i>k}$ $(\equiv A)$ are equal to those using the single-ion anisotropy $A_{i=k}$ $(= 3A)$. Therefore, the

resulting spin-wave spectra exhibiting anisotropy gap will also be indistinguishable. Regardless whether the spin gap is induced by single-ion or magnetic exchange anisotropy, the microscopic origin is the strong SOC induced by Cr-I interaction in CrI_3. Since the CrI_6 octahedra has little structural distortions below T_C [14], anisotropic Heisenberg exchange due to the SOC via Cr $3d$-I p-Cr $3d$ superexchange path interaction is likely responsible for the FM order in CrI_3 [12, 13].

Another possible mechanism that can provide spin anisotropy gap in honeycomb ferromagnets is the symmetric off-diagonal Γ term in the J-K-Γ Hamiltonian [18, 22, 23]. Whereas it also originates from the SOC, it is unlikely to be strong unless the diagonal K term is predominant. Although the J-K-Γ Hamiltonian with dominant Kitaev exchanges ($K/J = 25$) [18] fails to describe the spin-wave spectra, a reasonable fit to the full spectrum may be obtained when the next neighbor magnetic exchange J_2 is allowed to be similar to J_1 [23].

In conclusion, we used INS to show that the stiffness of the intraplanar and interplanar spin waves of CrI_3 has a finite value at T_C. While these results are contrary to the expectation of a 3D Heisenberg Hamiltonian with second order FM phase transition, they are consistent with our careful critical magnetic scattering measurements suggesting that the FM phase transition in CrI_3 is a weakly first order transition. Since the anisotropy gap is fully closed at T_C following similar temperature dependence as the order parameter, we conclude that the anisotropic SOC plays a decisive role in the FM phase transition in 3D CrI_3, and is responsible for stabilizing the FM order in monolayer CrI_3. We are not aware a ferromagnet where the Curie temperature is controlled by SOC instead of the magnetic exchange coupling. Since spin waves in a ferromagnet are Goldstone modes, they are more unstable than spin waves in an antiferromagnet if there is no magnetic anisotropy. For example, it is well-known that spin-wave-like excitations can appear above T_N in antiferromagnets, and temperature dependence of anisotropy gap follows the magnetic ordering parameter [50, 51]. By judicially adjusting the strength of SOC in 2D materials, one can control T_C of the system [32–36]. While monolayer CrI_3 orders ferromagnetically at $T_C \approx 45$ K [8], monolayer $CrBr_3$ can only order $T_C \approx 34$ K due to the reduced SOC [52], and long-range FM order will probably not survive in monolayer $CrCl_3$.

* jaehc@korea.ac.kr
† pdai@rice.edu

[1] M. Gibertini, M. Koperski, A. F. Morpurgo, and K. S. Novoselov, Nat. Nano. **14**, 408 (2019).
[2] S. Lovesey in *Theory of Thermal Neutron Scattering from Condensed Matter.* (Clarendon, Oxford, 1984), Vol. 2.
[3] Jiandi Zhang, F. Ye, Hao Sha, Pengcheng Dai, J. A. Fernandez-Baca, and E. W. Plummer, J. Phys.: Condens. Matter **19**, 315204 (2007).
[4] M. Collins in *Magnetic Critical Scattering (Clarendon, Oxford)*, (1989).
[5] N. D. Mermin and H. Wagner, Phys. Rev. Lett. **17**, 1133 (1966).
[6] M. T. Hutchings, J. Als-Nielsen, P. A. Lindgard, and P. J. Walker, J. Phys. C: Solid State Phys. **14**, 5327 (1981).
[7] H. E. Stanley and T. A. Kaplan, Phys. Rev. Lett. **17**, 913 (1966).
[8] B. Huang, G. Clark, E. Navarro-Moratalla, D. R. Klein, R. Cheng, K. L. Seyler, D. Zhong, E. Schmidgall, M. A. McGuire, D. H. Cobden, W. Yao, D. Xiao, P. Jarillo-Herrero, and X. Xu, Nature **546**, 270 (2017).
[9] C. Gong, L. Li, Z. Li, H. Ji, A. Stern, Y. Xia, T. Cao, W. Bao, C. Wang, Y. Wang, Z. Q. Qiu, R. J. Cava, S. G. Louie, J. Xia, and X. Zhang, Nature **546**, 265 (2017).
[10] C. M. Wynn, M. A. Gîrtu, W. B. Brinckerhoff, K.-I. Sugiura, J. S. Miller, and A. J. Epstein, Chem. Mater. **9**, 2156 (1997).
[11] B. D. Cullity and C. D. Graham, *Introduction to Magnetic Materials.* (John Wiley & Sons, 2005).
[12] J. L. Lado and J. Fernández-Rossier, 2D Materials **4**, 035002 (2017).
[13] Dong-Hwan Kim, Kyoo Kim, Kyung-Tae Ko, JunHo Seo, Jun Sung Kim, Tae-Hwan Jang, Younghak Kim, Jae-Young Kim, Sang-Wook Cheong, and Jae-Hoon Park, Phys. Rev. Lett. **122**, 207201 (2019).
[14] M. A. McGuire, H. Dixit, V. R. Cooper, and B. C. Sales, Chem. Mater. **27**, 612 (2015).
[15] Jeffrey G. Rau, Eric Kin-Ho Lee, and Hae-Young Kee, Phys. Rev. Lett. **112**, 077204 (2014).
[16] Heung-Sik Kim, Vijay Shankar V., Andrei Catuneanu, and Hae-Young Kee, Phys. Rev. B **91**, 241110(R) (2015).
[17] P. Peter Stavropoulos, D. Pereira, and Hae-Young Kee, Phys. Rev. Lett. **123**, 037203 (2019).
[18] I. Lee, F. G. Utermohlen, K. Hwang, D. Weber, C. Zhang, J. V. Tol, J. E. Goldberger, N. Trivedi, and P. C. Hammel, Phys. Rev. Lett. **124**, 017201 (2020).
[19] Changsong Xu, Junsheng Feng, Hongjun Xiang, and Laurent Bellaiche, npj Comp. Mater. **4**, 57 (2018).
[20] Moumita Deb and Asim Kumar Ghosh, J. Phys.: Condens. Matter **31**, 345601 (2019).
[21] Darshan G. Joshi, Phys. Rev. B **98**, 060405(R) (2018).
[22] P. Lampen-Kelley, S. Rachel, J. Reuther, J.-Q. Yan, A. Banerjee, C. A. Bridges, H. B. Cao, S. E. Nagler, and D. Mandrus, Phys. Rev. B **98**, 100403(R) (2018).
[23] See supplementary information for additional data and analysis.
[24] N. Richter, D. Weber, F. Martin, N. Singh, U. Schwingenschlögl, B. V. Lotsch, and M. Kläui, Phys. Rev. Mater. **2**, 024004 (2018).

[25] J. W. Lynn, R. W. Erwin, J. A. Borchers, Q. Huang, A. Santoro, J-L. Peng, and Z. Y. Li, Phys. Rev. Lett. **76**, 4046 (1996).
[26] J. A. Fernandez-Baca, P. Dai, H. Y. Hwang, C. Kloc, and S-W. Cheong, Phys. Rev. Lett. **80**, 4012 (1998).
[27] J. H. E. Griffiths, Nature (London) **158**, 670 (1946).
[28] A. T. Abdalian, B. Briat, C. Dugautier, and P. Moch, J. Phys. C: Solid State Phys. **20**, 2465 (1987).
[29] J. F. Dillon and C. E. Olson, J. Appl. Phys. **36**, 1259 (1965).
[30] Wencan Jin, Hyun Ho Kim, Zhipeng Ye, Siwen Li, Pouyan Rezaie, Fabian Diaz, Saad Siddiq, Eric Wauer, Bowen Yang, Chenghe Li, Shangjie Tian, Kai Sun, Hechang Lei, Adam W. Tsen, Liuyan Zhao, and Rui He, Nat. Comm. **9**, 5122 (2018).
[31] Lebing Chen, Jae-Ho Chung, Bin Gao, Tong Chen, Matthew B. Stone, Alexander I. Kolesnikov, Qingzhen Huang, and Pengcheng Dai, Phys. Rev. X **8**, 041028 (2018).
[32] Yujun Deng, Yijun Yu, Yichen Song, Jingzhao Zhang, Nai Zhou Wang, Zeyuan Sun, Yangfan Yi, Yi Zheng Wu, Shiwei Wu, Junyi Zhu, Jing Wang, Xian Hui Chen, and Yuanbo Zhang, Nature **563**, 94 (2018).
[33] Zaiyao Fei, Bevin Huang, Paul Malinowski, Wenbo Wang, Tiancheng Song, Joshua Sanchez, Wang Yao, Di Xiao, Xiaoyang Zhu, Andrew F. May, Weida Wu, David H. Cobden, Jiun-Haw Chu, Xiaodong Xu, Nature Materials **17**, 778 (2018).
[34] Manuel Bonilla, Sadhu Kolekar, Yujing Ma, Horacio Coy Diaz, Vijaysankar Kalappattil, Raja Das, Tatiana Eggers, Humberto R. Gutierrez, Manh-Huong Phan, Matthias Batzill, Nature Nanotechnology **13**, 289 (2018).
[35] D. J. OHara, T. Zhu, A. H. Trout, A. S. Ahmed, Y. K. Luo, C. H. Lee, M. R. Brenner, S. Rajan, J. A. Gupta, D. W. McComb, and R. K. Kawakami, Nano Letters **18**, 3125 (2018).
[36] M. Gibertini, M. Koperski, A. F. Morpurgo, and K. S. Novoselov, Nat. Nanotechnology **14**, 408 (2019).
[37] R. I. Bewley, J. W. Taylor, S. M. Bennington, Nuclear Instruments and Methods in Physics **637**, 128 (2011).
[38] R. A. Ewings, A. Buts, M. D. Le, J. van Duijn, I. Bustinduy, T. G. Perring, Nuclear Instruments and Methods in Physics Research A **834**, 132 (2016).
[39] Heinz Maier-Leibnitz Zetrum, Journal of Large-Scale Research Facilities, **1**, A12 (2015).
[40] D. H. Yu, R. Mole, T. Noakes, S. Kennedy, and R. Robinson, J. Phys. Soc. Jpn. **82**, SA027 (2013).
[41] G. E. Granroth, A. I. Kolesnikov, T. E. Sherline, J. P. Clancy, K. A. Ross, J. P. C. Ruff, B. D. Gaulin, S. E. Nagler, Journal of Physics: Conference Series **251**, 12058 (2010).
[42] Barry Winn, Uwe Filges, V. Ovidiu Garlea, Melissa Graves-Brook, Mark Hagen, Chenyang Jiang, Michel Kenzelmann, Larry Passell, Stephen M. Shapiro, Xin Tong, and Igor Zaliznyak, EPJ Web of Conferences **83**, 03017 (2015).
[43] M. A. McGurie, Crystal **7**, 121 (2017).
[44] A. R. Wildes, H. M. Rønnow, B. Roessli, M. J. Harris, and K. W. Godfrey, Phys. Rev. B **74**, 094422 (2006).
[45] E. J. Samuelsen, R. Silberglitt, G. Shirane, and J. P. Remeika, Phys. Rev. B **3**, 157 (1971).
[46] T. J. Williams, A. A. Aczel, M. D. Lumsden, S. E. Nagler, M. B. Stone, J.-Q. Yan, and D. Mandrus, Phys. Rev. B **92**, 144404 (2015).
[47] R. J. Birgeneau, M. Greven, M. A. Kastner, Y. S. Lee, B. O. Wells, Y. Endoh, K. Yamada, and G. Shirane, Phys. Rev. B **59**, 13788 (1999).
[48] G. T. Lin, X. Luo, F. C. Chen, J. Yan, J. J. Gao, Y. Sun, W. Tong, P. Tong, W. J. Lu, Z. G. Sheng, W. H. Song, X. B. Zhu and Y. P. Sun, Appl. Phys. Lett. **112**, 072405 (2018).
[49] S. Toth and B. Lake, Journal of Physics: Condensed Matter. **27**, 16 (2015).
[50] H. W. de Wijn, L. R. Walker, S. Geschwind, and H. J. Guggenheim, Phys. Rev. B **8**, 299 (1973).
[51] Franz Demmel and Tapan Chatterji, Phys. Rev. B **76**, 212402 (2007).
[52] Zhaowei Zhang, Jiangzhi Shang, Chongyun Jiang, Abdullah Rasmita, Weibo Gao, and Ting Yu, Nano Lett. **19**, 3138 (2019).

ACKNOWLEDGMENTS

We are grateful to R. J. Birgeneau and Andriy Nevidomskyy for helpful disucssions. The INS and single crystal synthesis work at Rice was supported by the U.S. NSF Grant No. DMR-1700081 and the Robert A. Welch Foundation Grant No. C-1839 (P.D.), respectively. The work of J.-H.C. was supported by the National Research Foundation of Korea (No. NRF-2016R1D1A1B03934157; No. NRF2017K1A3A7A09016303). A portion of this research used resources at the Spallation Neutron Source, a DOE Office of Science User Facility operated by ORNL. Experiments at the ISIS Neutron and Muon Source were supported by a beam time allocation RB1820251 from the Science and Technology Facilities Council.

Supplemental Information:
Magnetic anisotropy in ferromagnetic CrI_3

In the following, we present the raw data where the conclusions in the main text are reached and discussed in detail on Kitaev and Heisenberg Hamiltonian calculations. Figure S1 shows constant-energy scans at different wave vectors along the [H, H, 0] direction at different temperatures from the PANDA measurements. The blue lines in the figure are fits using the simple quadratic relationship discussed in the main text. Fig. S1(g) shows temperature dependence of the spin gap. Here the values of the spin gap estimated from the fits are larger than those obtained using the c-axis spin wave dispersion because of the relatively poor instrumental resolution and large uncertainty using constant-energy fits to obtain the spin wave dispersion. Nevertheless, the temperature dependence of the spin gap reveals similar behavior as those obtained from the c-axis dispersion shown in the main text. Figure S2 shows the raw data obtained on PANDA at different temperatures. Figure S3 shows spin wave dispersions calculated using different models.

Experimental

We carried out some of the measurements using the LET neutron time-of-flight instrument as discussed in the main text. The experiments were with multi-E_i (incident beam energy) mode (E_i = 25 meV, 5.37meV [Fig. 1(f)] and 2.27meV [Fig. 2(a)]) with sample fixed at 3 K. A Horace scan was done on co-aligned 0.42 g single crystals of CrI_3 with the sample in the [H,H,L] scattering plane.

The PANDA is a cold neutron triple-axis spectrometer as described in the main text. The experiments were carried out with a fixed final neutron energy of E_f = 3.78 meV. Constant-E scans were performed along the [H,H,3] direction at temperatures of 2 K, 30 K, 50 K, 57 K, 59 K, 61 K, 63 K, 68 K, 73 K, 78 K, 84 K, and 250 K. Constant-**Q** scans are performed at **Q** = (0 0 2.25) and (0 0 4.5) with sample temperatures of 2 K, 30 K, 50 K, 57 K and 59 K [Fig. 2(c)(d)]. The sample mass is 0.84 g of co-aligned single crystals of CrI_3. To get the anisotropy gap Δ and D_L which is proportional to the [0 0 L] bandwidth E_{band}, we used $E_{band} = 2(E_{4.5} - E_{2.25})$, and $\Delta = E_{4.5} - E_{band}$ to get the Δ and D_L in Fig. 2(f). This method is equal to a simple sinusoidal fit.

The SEQUOIA instrument is a neutron time-of-flight spectrometer as discussed in the main text. Our experiments on SEQUOIA were carried out with E_i = 25 meV [Fig. 3(a-d)] and 8 meV [Fig. 3(e)(f)] at temperatures 5 K, 52 K, 63 K, and 70 K (Fig. S4). Horace scans are done on co-aligned ~0.2 g single crystals of CrI_3 with the sample in the [H,0,L] scattering plane. The 0.6meV flat mode in Fig.3(e)(f) is an instrumental artifact.

The HYSPEC experiments were performed on ~6 g powder samples at 3 K [fig.S7(a)]. A Horace scan is performed to eliminate the anisotropy inside the powder sample.

The Pelican experiments were performed on ~14 g powder samples at 2K, 50K ,55K and 57K.Two incident energies, 3.7meV [fig. S5(c)] and 2.3meV [fig. S5(b)], were used to probe the anisotropy gap located at (0 0 3) (q_{gap} = 0.96Å^{-1}). The anisotropy gap value is extracted by subtracting the

integrated intensity at range [q_{gap}-0.05, q_{gap}+0.05] Å^{-1} by an average of the intensity at [q_{gap}-0.35, q_{gap}-0.25] Å^{-1} and [q_{gap}+0.25, q_{gap}+0.35] Å^{-1} [See fig. S5(a)].

We use Takin[S2] as a convolutional fitting tool on PANDA data shown on Fig.2 (c)(d). The fitting parameters include an intensity scale factor, and the spin wave energy for each scan. We use the same method indicated before ($E_{band} = 2(E_{4.5} - E_{2.25})$, $\Delta = E_{4.5} - E_{band}$) to get the [0 0 L] bandwidth and the anisotropy gap. The result is shown in Fig. S6. No obvious changes have been observed in the temperature dependence of D_L and Δ after the convolutional fitting.

The magnetic critical scattering is measured on the HB-3 thermal neutron triple axis spectrometer at High-Flux Isotope Reactor, Oak Ridge National Laboratory [Fig. 4(a)-(g)]. The monochromator, analyzer, and filter are pyrolytic graphite (PG). For triple-axis measurements, final neutron energy of 14.7 meV was used and a PG filter was placed after the sample. For two-axis measurements, a PG filter was placed before the sample to reduce λ/2 and incident neutron energy was set at 30.5 meV. A single piece of CrI_3 single crystal (13 mg) with mosaic < 1 degree was used in the experiment.

Comparison of neutron Time-of-Flight measurements and calculations on powder CrI_3

The simulation uses linear spin wave theory with the SpinW software developed by PSI [S1]. For the powder spectra shown in Fig. S7(b-d), the code chooses random orientation 1000 times to get an averaged intensity distribution.

Heisenberg model Hamiltonian with DM interaction is:

$$H = -\sum_{i<j}[J_{ij}\boldsymbol{S_i}\cdot\boldsymbol{S_j} + A_{ij}\cdot(\boldsymbol{S_i}\times\boldsymbol{S_j})] - \sum_j D_z(s_j^z)^2 \qquad (1)$$

as in ref. [31], with intralayer term J_1 = -2.13 meV, J_2 = -0.09 meV, J_3 = 0.10 meV, interlayer term J_c = -0.59 meV and anisotropy term D_z = -0.20 meV. For the choice of the DM term A_{ij}, we used 0.194 meV in the calculation in Fig. S7(b). The DM term in ref. [31] (~0.31 meV) is overestimated due to the sample mosaic.

Heisenberg-Kitaev (J-K-Γ) model Hamiltonian:

$$H = -\sum_{\langle ij\rangle\in\lambda\mu(\nu)}[J\boldsymbol{S_i}\cdot\boldsymbol{S_j} + KS_i^\nu S_j^\nu + \Gamma(S_i^\lambda S_j^\mu + S_i^\mu S_j^\lambda)] \qquad (2)$$

For the simulation reproducing ref. [18], we chose J_1 = -0.212meV for the Heisenberg term, K = -5.19meV for the Kitaev term, and Γ = -0.0675meV for the symmetric off-diagonal anisotropy. (λ, μ, ν) = any permutation of (x, y, z). The interlayer interaction is ignored which turns out to be small and not influential to the simulation results in Figs. S7(c) and S7(e). Figures S3(a) and S3(b) compare our calculation with those from [18]. Data and calculation for Heisenberg model and Kitaev model are shown in Figs. S3(c), (d) and (e), respectively.

As shown in Fig. S7(e), the model reproducing ref. [18] is clearly not consistent with the powder neutron scattering data. To make optimal simulation using the J-K−Γ model, we fit the INS data

in [31] with the J-K−Γ model, and the fitting result gives J1 = -0.17meV, J2 = -0.21meV, K = -5.6meV, and Γ = -0.075meV. Using these parameters, we get the simulation results in Fig. S7(d) and S7(e). These results suggest that the H-K model can have parameters regimes, similar to the Heisenberg-DM model in ref. [31], that can describe the observed inelastic neutron scattering spectra in CrI_3. The parameters are similar to that in ref.[18], whereas the introduction of J_2 shifts the Dirac gap from 5~8meV to 10~13meV.

Figures

Constant-E scans at 2~250K

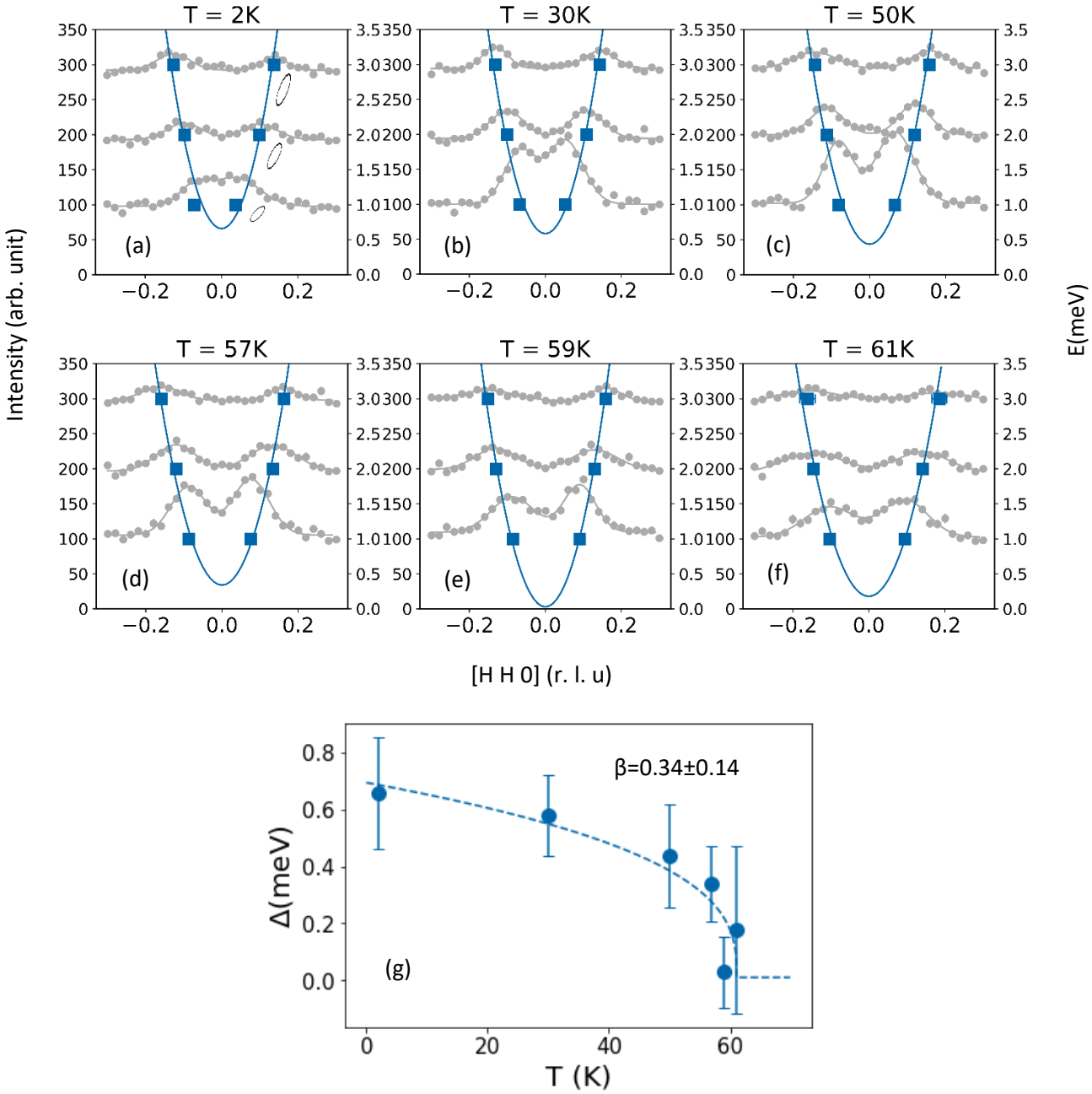

Fig. S1: (a-f) Const-E scan on [H H 0] under 2K, 30K, 50K, 57K, 59K and 61K. The gray points and curves are raw data and Gaussian fits, respectively; the blue ones are parabolic fit of the dispersion. The ellipses in (a) is the instrument resolution ellipse at 1, 2 and 3meV. (g) Temperature dependence of the anisotropy gap size from the fit in (a-f). The blue dashed line is a power law fit ($E = A(1-T/T_c)^{\beta}$) which gives β=0.34±0.14.

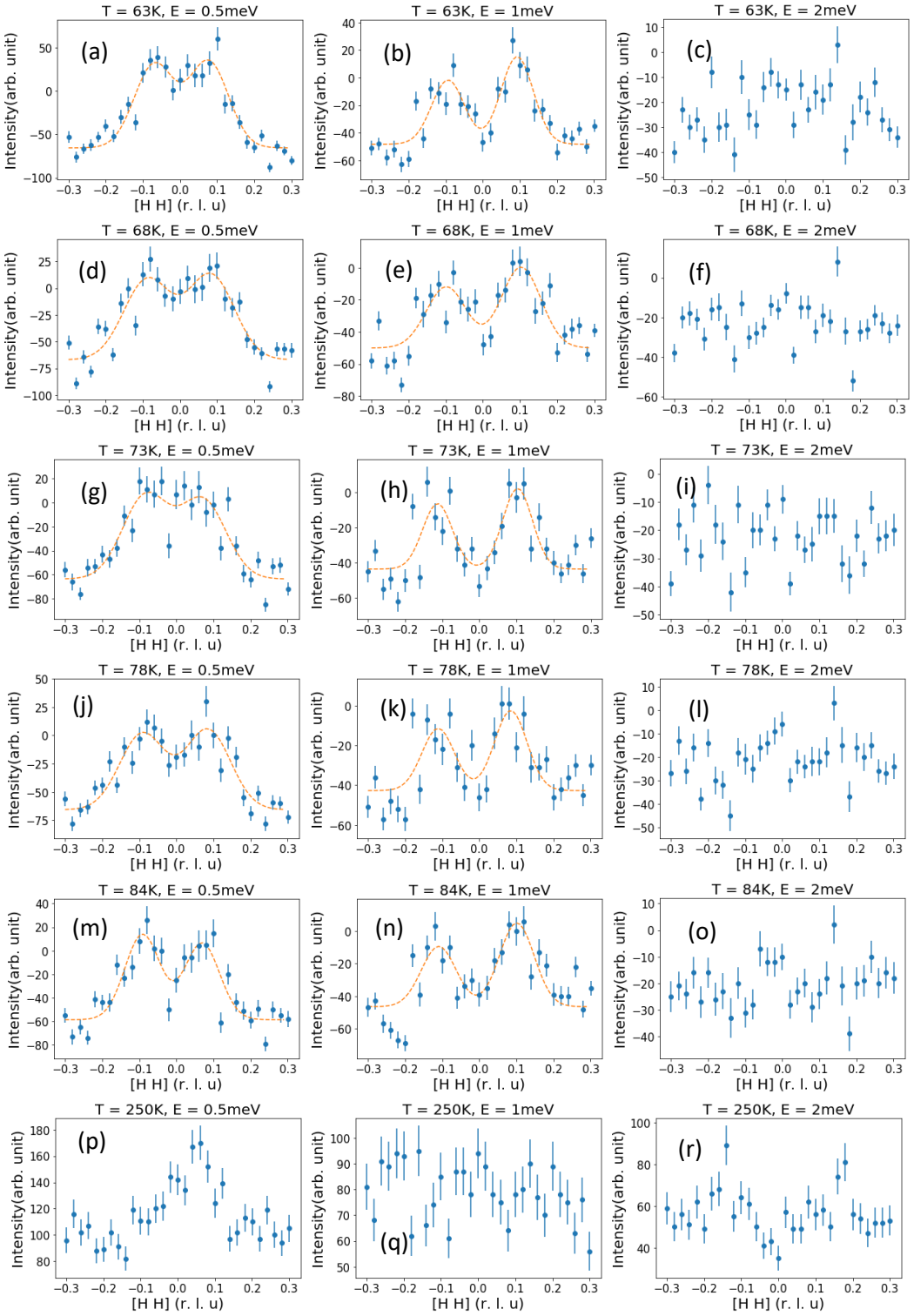

Fig. S2: Const-E scan on [H H 0] plane under 63K, 68K, 73K, 78K, 84K and 250K at 0.5, 1 and 2meV. (a-o) show the data with subtracted "backgrounds" collected at 250K, which are shown in (p-r). Orange lines are Gaussian fits.

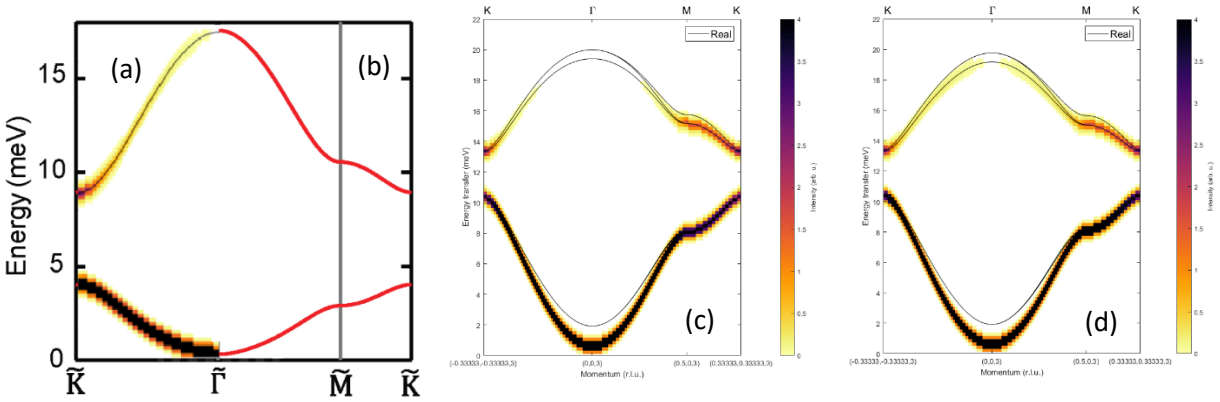

Fig. S3: Single crystal spin-wave dispersion corresponding to (a) reproduction to ref. [18]; (b) Fig. 4(d) in ref. [18]; (c) Heisenberg model in ref. [31] with minor correction on DM term; (d) J-K-Γ model simulation from this work [see Fig. 4(d)].

Spin excitations in high Temperature

Figures S4 summarizes data obtained at temperatures near and above Curie temperature. Data are obtained on SQUOIA with incident energy of 25 meV.

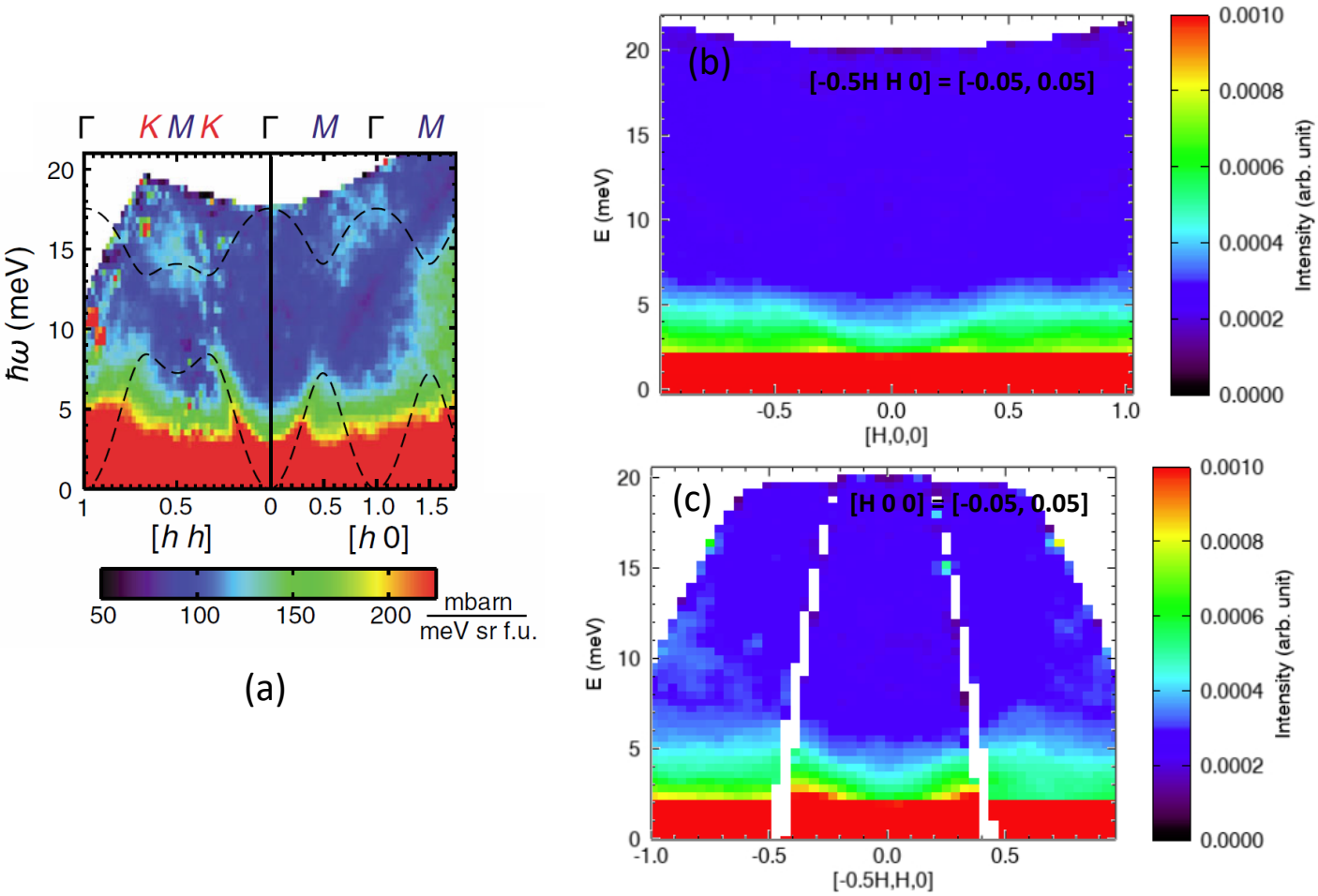

Fig. S4: Spin excitations at (a) 52K (ref. [31]); (b) 70 K along [H 0] (Γ-M); (c) 70 K along [-0.5H H] (Γ-K). All integrated with [0 0 L] = [-5, 5].

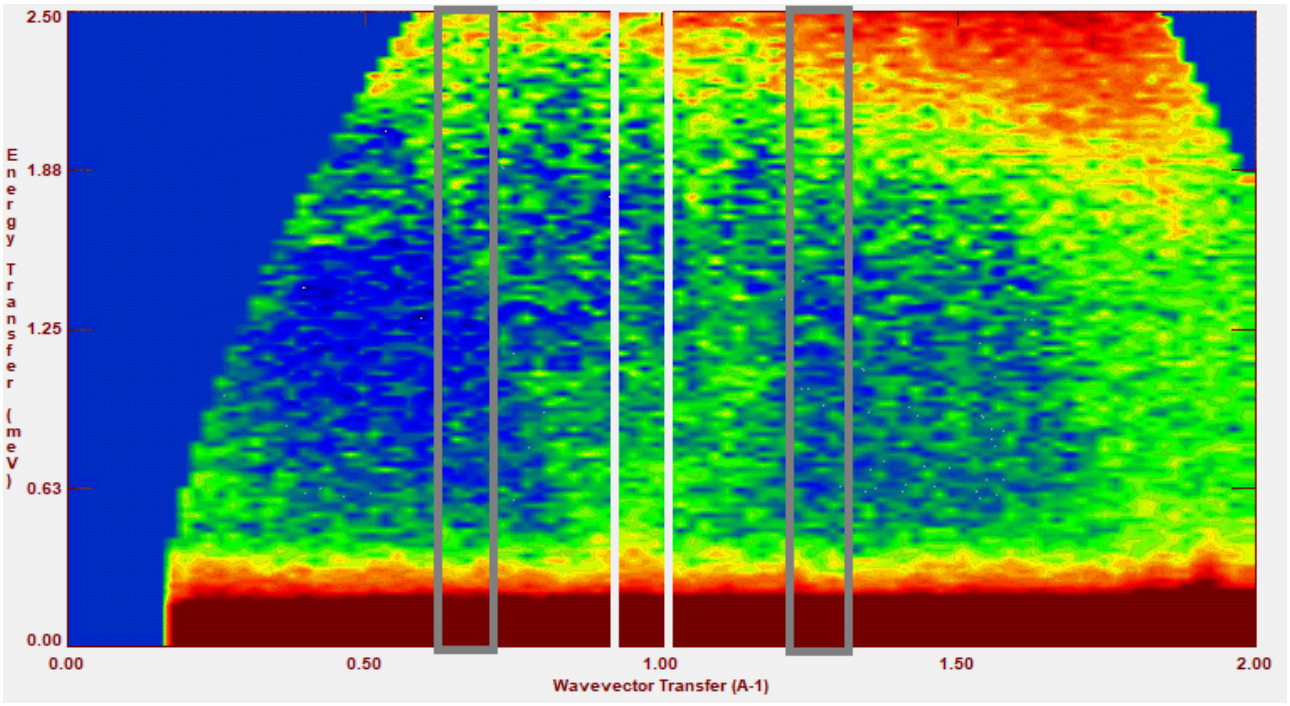

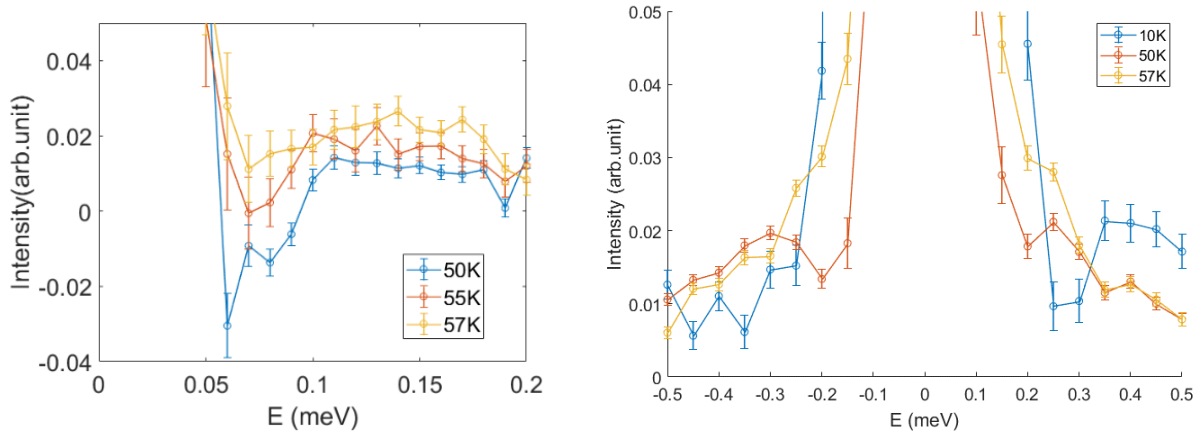

Fig. S5: (a) Low energy powder spectrum of CrI_3 at 10K, data plots in (b) and (c) are calculated by (intensity in white square) – (averaged intensity in gray squares). (b) Raw data plots using E_i = 2.3meV at 50K, 55K and 57K; (b) Raw data plots using E_i = 3.7meV at 10K, 50K and 57K. The 10K intensity is multiplied by 5 for clarity; the 50 and 57K data is subtracted by 10K data to get rid of the (0 0 3) elastic peak.

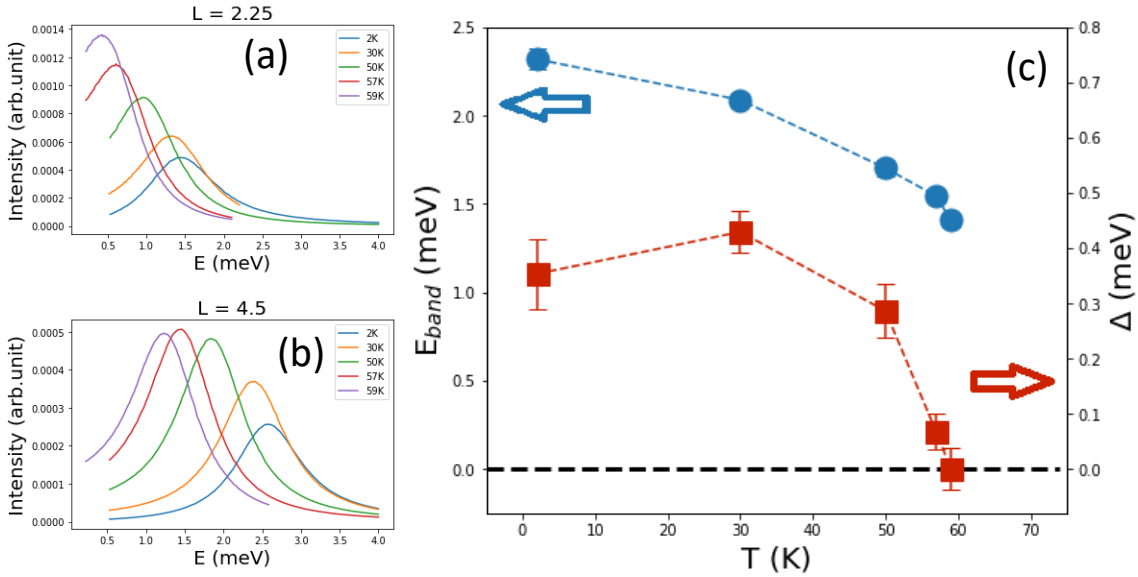

Fig. S6: Convolutional fit result of [0 0 L] scans. (a)(b) The convoluted energy scans for fig. 2(c)(d) in the main text, respectively. (c) Convoluted fit of the [0 0 L] bandwidth and anisotropy gap. The blue circles are calculated [0 0 L] bandwidth which is proportional to D_L in the main text; Red squares are calculated gap value. Note that the gap values have been shifted in order to match the LET data (0.34meV at 3K).

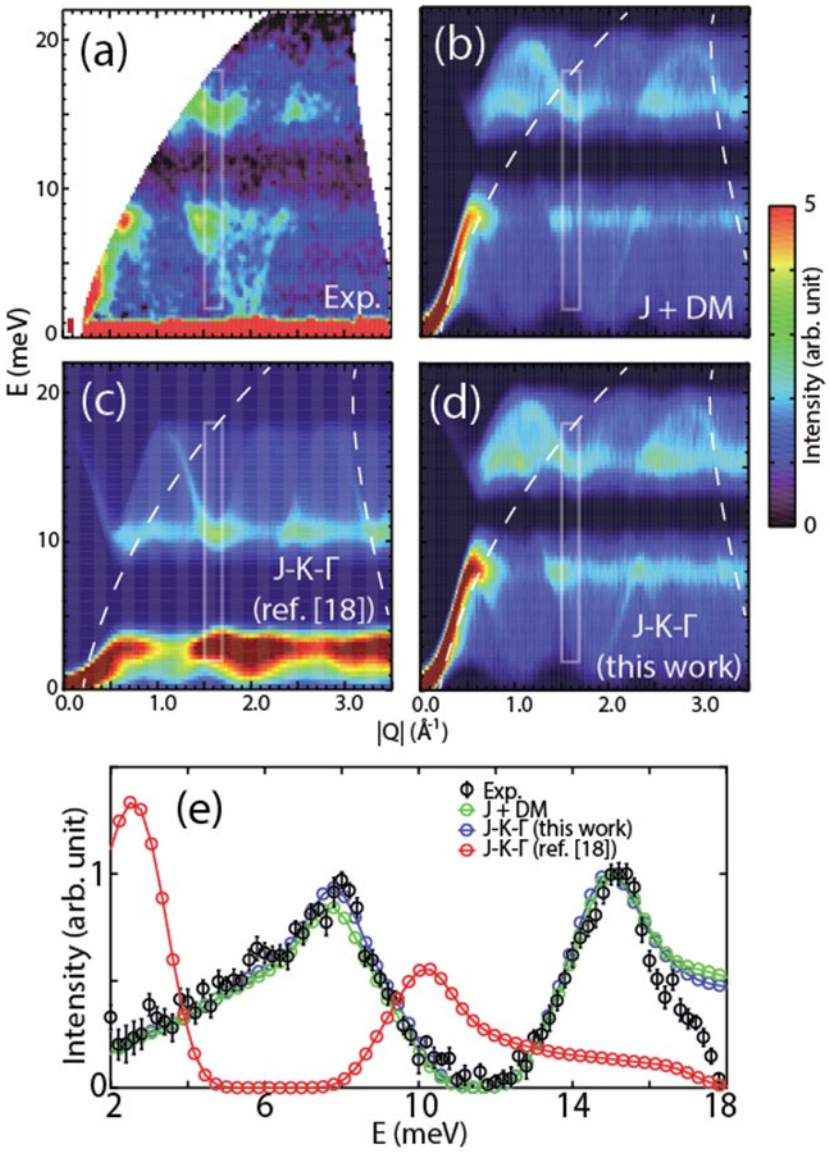

Fig. S7. (a) Experimental powder magnon spectrum of CrI_3 at T = 5K using E_i = 25meV. (b, c, d) Powder-averaged spin-wave spectra calculated using the Heisenberg-DM [31], J-K-Γ Hamiltonian using parameters of Ref.[18], and new parameters (J1=−0.17±0.05 meV,J2=−0.21±0.04 meV, K=−5.6±0.2 meV), respectively. The dashed lines mark the limits of the data in (a). (e) The black, green, red, and blue points/lines are the experimental data, Heisenberg-DM, J-K-Γ Hamiltonian calculations with parameters of [18] and the new parameters mentioned above, respectively. The scan directions are marked as solid boxes in (a-d).

References

[S1] S. Toth and B. Lake. Journal of Physics: Condensed Matter, Vol 27, 16 (2015)

[S2] T. Weber, SoftwareX, Volume 5, 121-126 (2016)